Origin and Episodic Emplacement of the Manaslu Intrusive Complex, Central Himalaya

T. MARK HARRISON[1]*, MARTY GROVE[1], KEVIN D. McKEEGAN[1], C. D. COATH[1], OSCAR M. LOVERA[1] AND PATRICK LE FORT[2]

[1]DEPARTMENT OF EARTH AND SPACE SCIENCES AND INSTITUTE OF GEOPHYSICS AND PLANETARY PHYSICS, UNIVERSITY OF CALIFORNIA, LOS ANGELES, CA 90095-1567, USA

[2]CNRS, INSTITUT DOLOMIEU, 38301 GRENOBLE, FRANCE

The Manaslu granite is the most studied of the dozen or so plutons that make up the High Himalayan leucogranite belt. The inferred relationship of the Manaslu granite with important Himalayan tectonic structures has inspired repeated attempts to determine its crystallization age, but several geochemical controls have hampered these geochronological investigations. These limitations are circumvented by Th–Pb ion microprobe dating of monazite. We have determined 158 Th–Pb ages on monazites separated from 11 samples of the Manaslu leucogranite. Together with an earlier published datum, these results indicate that the Manaslu intrusive complex was constructed during pulses of magmatism at $22\cdot9 \pm 0\cdot6$ Ma (Larkya La phase) and $19\cdot3 \pm 0\cdot3$ Ma (Bimtang phase). Monazite Th–Pb results for a single sample of the Dolpo-Mugu granite, located 75 km NW of the Manaslu intrusive complex, yield an age of $17\cdot6 \pm 0\cdot3$ Ma and suggest a protracted (~0·5 my) magmatic history that appears unrelated to the two phases of Manaslu magmatism. Age constraints on the emplacement of the Manaslu intrusive complex require that extensional structures cut by the Manaslu intrusive complex be 23–19 Ma or older. Geochemical constraints are consistent with the Larkya La phase of magmatism resulting from muscovite dehydration melting. The available timing and geochemical constraints are consistent with the Bimtang phase being produced from a higher-temperature pulse of dehydration melting. Thermo-kinematic modeling indicates that (1) two phases of leucogranite magmatism separated by ~4 my can be produced by shear heating along the Himalayan décollement assuming a shear stress of 45 MPa, and (2) scenarios involving only decompression to achieve the same result appear to require extreme conditions not permitted by available geological constraints.

INTRODUCTION

The High Himalayan leucogranites are a discontinuous chain of sheet-like plutons and dikes that extend along the crest of the Himalayan range (Fig. 1). Their possible interrelationship with both the Main Central Thrust (MCT) and South Tibetan Detachment System (STDS), arguably the two most significant tectonic features of that mountain belt (Fig. 1), has inspired several competing petrotectonic models. The classical interpretation that the High Himalayan leucogranites formed from fluid-induced anatexis of MCT hanging-wall rocks, triggered by devolatilization of overthrust footwall rocks in concert with shear heating (e.g. Le Fort, 1975; England *et al.*, 1992), has been challenged by the view that the leucogranites instead formed by dehydration melting induced during decompression caused by slip on the STDS (e.g.
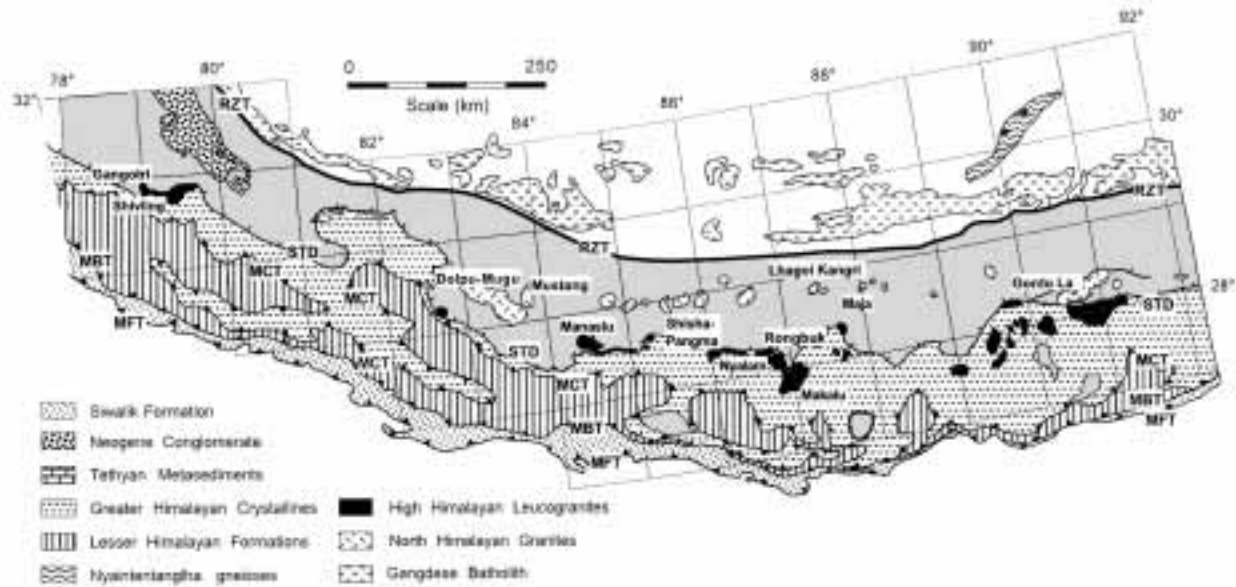
Fig. 1. Geologic sketch map of the Himalaya showing the locations of the High Himalayan and North Himalayan magmatic belts. Labeled plutons are those for which U–Th–Pb monazite ages are available. Data sources are: Gangotri (22·4 ± 0·5 Ma, Harrison *et al.*, 1997*a*), Shivling (21·9 ± 0·5 Ma; Harrison *et al.*, 1997*a*), Manaslu (22·9 ± 0·6 and 19·3 ± 0·3 Ma; Harrison *et al.*, 1995*b*; this study), Everest–Makalu (23 ± 1 Ma; Schärer, 1984), Shisha-Pangma (20–17 Ma; Searle *et al.*, 1997), Nyalam (16·8 ± 0·6 Ma; Schärer *et al.*, 1986), Khula Kangri (12·5 ± 0·5 Ma; Edwards & Harrison, 1997); Dolpo-Mugu (17·6 ± 0·3 Ma; this study), Lhagoi Kangri (15·1 ± 0·5 Ma; Schärer *et al.*, 1986), and Maja (9·5 ± 0·5; Schärer *et al.*, 1986). MFT, Main Frontal Thrust; MBT, Main Boundary Thrust; MCT, Main Central Thrust; RZT, Renbu Zedong Thrust; STD, South Tibetan Detachment.

Harris *et al.*, 1993; Guillot & Le Fort, 1995). This paradigm shift carries the implication that anatexis immediately followed substantial displacement along the STDS, but may not have been synchronous with motion on the MCT. If anatexis resulted from slip on the MCT, leucogranite crystallization ages provide a lower bound on the initiation of Himalayan thrusting. Although geochronological investigations suggest that the MCT hanging wall was actively deforming at ~22 Ma (e.g. Hodges *et al.*, 1996), the age of MCT initiation is poorly known (England *et al.*, 1992). Recent evidence indicates that the MCT ramp was reactivated during the late Miocene (Harrison *et al.*, 1997*b*) and that early Miocene anatexis occurred immediately above the basal décollement of the Himalayan thrusts rather than along the ramp (Harrison *et al.*, 1997*a*). If instead anatexis was driven by decompression melting caused by tectonic denudation, establishing the timing of emplacement of these intrusions constrains the displacement history of the STDS. Determining the deformation histories of these Himalayan master faults should permit better assessment of contrasting mechanical models that causally relate MCT thrusting and STDS extension (e.g. Burg *et al.*, 1984; Burchfiel & Royden, 1985; Yin, 1993).

Although the tectonic significance of the High Himalayan leucogranites motivated numerous geochronological studies, these rocks have proven challenging to date. Because of the paucity of reliable crystallization ages, the few that have been obtained have been assumed to be representative of relatively large plutons that may in fact be composite bodies. Our goal in this paper is to exploit the recently developed monazite Th–Pb ion microprobe dating method (Harrison *et al.*, 1995*b*) to obtain the first detailed geochronology of a Himalayan leucogranite. Our results for the Manaslu granite document two phases of magmatism, constrain the ages of internal deformation that may be related to STDS activity, and provide the basis with which to investigate petrogenetic models of anatexis.

THE MANASLU GRANITE
Geological setting

The Manaslu granite, the most thoroughly studied of all the High Himalayan leucogranites (e.g. Le Fort, 1975, 1981; Vidal, 1978, 1982, 1984; Le Fort *et al.*, 1982, 1987; Deniel *et al.*, 1987; France-Lanord & Le Fort, 1988; France-Lanord *et al.*, 1988; Copeland *et al.*, 1990; Pêcher, 1991; Guillot *et al.*, 1993, 1994, 1995; Guillot & Le Fort, 1995; Harrison *et al.*, 1995*b*; Chen *et al.*, 1996), is a lenticular body of ~10 km maximum thickness that gently dips to the NNE with a relatively thin sheet, the Chhokang Arm, extending ~60 km to the east of the main body (Fig. 2). The granite is emplaced into, and cuts, a north-verging recumbent anticline developed within Tethyan
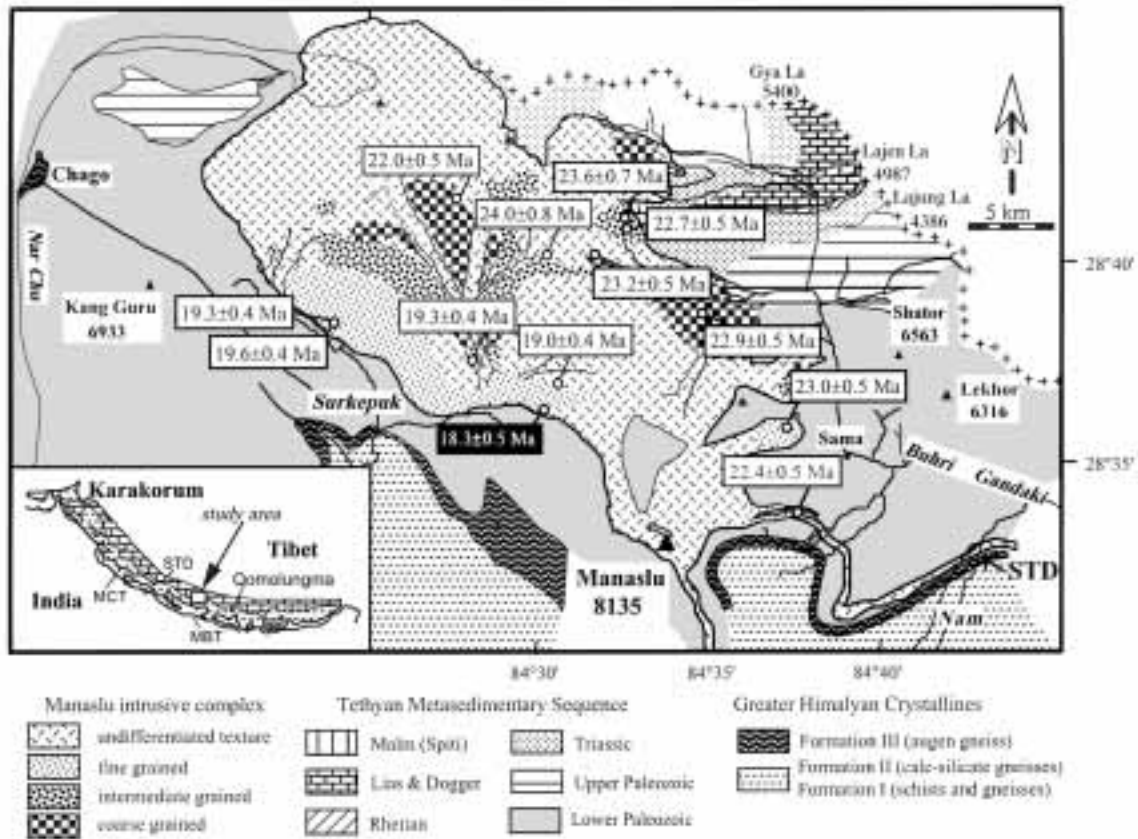
Fig. 2. Geological map of the Manaslu granite and surrounding region. Patterns within the main body of the granite designate the characteristic grain size. Interpreted crystallization ages from Th–Pb monazite dating are shown in the caption boxes. The location of the Rb–Sr isochron result of Deniel *et al.* (1987) is shown in the black caption box. (See Table 1 for sample identification.) The Nepal–Tibet border is indicated by crosses.

metasediments (Le Fort, 1981). The base of that fold is truncated by an STDS structure that is itself cut by granitic dikes. There is localized development within the pluton of ductile normal shear with a right lateral component indicating that internal deformation was occurring while the leucogranite was still at high temperature (Guillot *et al.*, 1993, 1995). Emplacement appears to be largely by dike intrusion with the depth of the roof zone estimated to be ~12 km (Guillot *et al.*, 1993, 1995). Beneath the STDS are gneisses of the Greater Himalayan Crystallines (GHC) that are themselves juxtaposed atop lower-grade schists of the Lesser Himalayan Formations by the south-directed MCT (Fig. 1). Based on its compositional and isotopic characteristics, the lowermost unit of the GHC (Formation I) is widely believed to represent the unmelted equivalent of the leucogranite source region (e.g. Le Fort, 1981; Barbey *et al.*, 1996).

The Manaslu granite is composed of two leucogranite types; a two-mica variety and a less abundant (~20%) tourmaline leucogranite (Guillot & Le Fort, 1995). The generally lower Rb/Sr and initial $^{87}Sr/^{86}Sr$ ratio ($^{87}Sr/$ $^{86}Sr_i$) of the two-mica leucogranite is broadly similar to that of peraluminous metagraywackes in the Greater Himalayan Crystallines and suggested to Guillot & Le Fort (1995) that these rocks were the source of melting. Those workers further proposed that the tourmaline leucogranites, which appeared to them to have higher average Rb/Sr and $^{87}Sr/^{86}Sr_i$ than the two-mica varieties, were derived via H_2O-undersaturated melting of GHC metapelites.

In general, the southwestern side of the pluton is characterized by a relatively fine grain size whereas the central and northeastern portions are generally coarser grained (Fig. 2). Although possibly a reflection in part of different levels of exposure of the laccolith, the textural contrasts between the northeastern and southwestern portions of the Manaslu granite are generally mimicked by several geochemical signatures. The coarser-grained central and northeastern portions of the pluton (Fig. 2) are associated with generally higher Rb/Sr (Fig. 3; see Table 2, below) higher $^{87}Sr/^{86}Sr_i$ (>0·752; Deniel *et al.*, 1987), and lower Th/U ratios (<0·7) relative to the
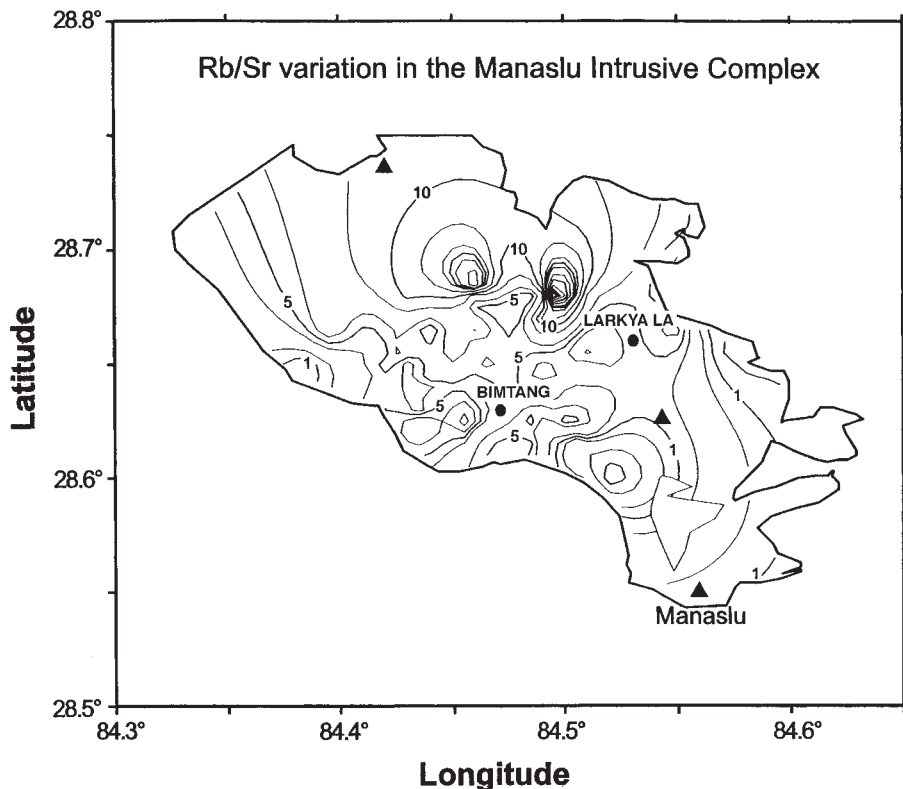
Fig. 3. Contour plot showing variation of Rb/Sr within the Manaslu granite. It should be noted that the southwestern portion of the pluton is characterized by lower Rb/Sr than the central and northeastern portions. Data are taken from Guillot (1993).

southwestern side (Guillot, 1993; see Table 2). An exception to this trend is a restricted region on the southwestern side of the pluton which, in contrast to the encompassing region, is characterized by $^{87}Sr/^{86}Sr_i$ ratios of >0·752 (Deniel *et al.*, 1987). We note that these spatially, texturally, and geochemically distinct units contain both two-mica and tourmaline leucogranite varieties.

Prior age constraints

Problems inherent in dating High Himalayan leucogranites are in general due to the minimum melt character of these magmas. Heterogeneous $^{87}Sr/^{86}Sr$ and $^{143}Nd/^{144}Nd$ initial ratios (e.g. Vidal *et al.*, 1982; Le Fort *et al.*, 1987) preclude whole-rock isochron dating of the Manaslu granite except in rare cases (e.g. Deniel *et al.*, 1987). U–Pb accessory mineral dating is complicated by the low solubilities of these phases in leucogranite magmas (Harrison & Watson, 1983; Montel, 1993) and the likelihood of their containing an inherited component (Copeland *et al.*, 1988). In general, leucogranite zircons are highly contaminated by inherited Pb* and only rarely appear to yield meaningful crystallization ages (e.g.

Schärer *et al.*, 1986). Igneous monazites commonly incorporate significant ^{230}Th during crystallization; this results in the production of unsupported $^{206}Pb*$ and obviates the advantages of U–Pb concordia. $^{40}Ar/^{39}Ar$ dating of the Manaslu granite and aureole yield either ~15–19 Ma cooling ages or older dates which reflect contamination by excess ^{40}Ar (e.g. Copeland *et al.*, 1990; Guillot *et al.*, 1994; Harrison & Mahon, 1995). Deniel *et al.* (1987) obtained a single conventional U–Pb monazite age for one Manaslu granite sample. The datum was slightly reversely discordant, because of the presence of unsupported $^{206}Pb*$, and thus the $^{207}Pb/^{235}U$ age of 25·7 Ma was interpreted as indicating the age of crystallization (Deniel *et al.*, 1987), a view that was later widely accepted (France-Lanord & Le Fort, 1988; Hodges *et al.*, 1988a; Le Fort, 1988; Pêcher, 1991; Chen *et al.*, 1994; Guillot *et al.*, 1994; Villa, 1996).

Harrison *et al.* (1995a) used $^{208}Pb/^{232}Th$ ion microprobe dating of monazite to constrain the crystallization age for one sample from the southeastern portion of the Manaslu pluton. Because of the short half-lives of the intermediate daughters of ^{232}Th, this approach has the advantage of being insensitive to problems of disequilibrium Pb*. Moreover, the spatial resolution of ion

microprobe analysis allows measurements of sub-domains of individual monazite crystals so that the question of homogeneity of calculated ages can be explicitly examined. The measurements reported by Harrison *et al.* (1995*a*) revealed the presence of a single inherited monazite crystal which yielded ages of ~600 Ma. This result cast doubt on the reliability of the Deniel *et al.* (1987) datum as representing the emplacement age and led Harrison *et al.* (1995*a*) to instead conclude that this rock crystallized at 22·4 ± 0·5 Ma. Despite the seeming clarity of this interpretation, several important questions remain. These include: Is the Manaslu granite homogeneous with respect to crystallization age? Could the single inherited grain be a laboratory contaminant? Is the 22·4 Ma age actually dating metamorphic monazite in the protolith rather than magmatic crystallization? In this paper, we follow up on our analysis of the single sample by presenting dating results of an additional 11 Manaslu granite samples and a neighboring pluton, the Dolpo-Mugu granite. We conclude that these results are consistent with the construction of the Manaslu granite during two phases of early Miocene magmatic activity separated in time by ~4 my, a lag interpreted to reflect the time necessary for the *P–T*–fluid conditions to alter sufficiently to trigger a second melting event in the same source region.

ANALYTICAL METHODS
Th–Pb ion microprobe analyses

The principal advantages of the ^{232}Th–^{208}Pb system over the U–Pb method for dating Tertiary monazites are the rapid attainment of secular equilibrium (~30 yr) and high (typically 3–8%) Th concentrations (Montel, 1993) resulting in very high levels of ^{208}Pb*. Uranium concentrations are typically between one and two orders of magnitude lower. The ion microprobe has the demonstrated potential to directly image, and thus avoid, inherited Pb* residing in restitic monazite cores (e.g. Harrison *et al.*, 1995*b*; Edwards & Harrison, 1997). Given that the melting temperature of Himalayan leucogranites is ~750°C (Montel, 1993; Scaillet *et al.*, 1995), the diffusion of Pb in monazite is sufficiently limited (Smith & Giletti, 1997) to assure a record of crystallization in the cores of >50 μm grains in rocks cooling at >50°C/my. The widespread observation of inheritance (Harrison *et al.*, 1995*b*; Edwards & Harrison, 1997; this study) confirms this expectation.

The relatively high ionization efficiency of Pb from monazite under O_2^- bombardment (~1% useful yield), coupled with high abundances of ^{208}Pb*, permits ^{208}Pb/^{232}Th age determinations to be made in an ~5 μm spot on a Tertiary specimen in ~20 min. Details of our analytical methods have been described by Harrison *et*

al. (1995*b*). A mass resolving power of ~4500 is adequate to separate all molecular interferences (mostly LREE(PO$_2$)$^+$) in the 204–208 mass range. Comparison of ion microprobe Pb isotopic measurements of a synthetic Pb-bearing monazite that was isotopically characterized by thermal ionization mass spectrometry indicates that instrumental mass discrimination is <1‰/ a.m.u.

Secondary ion emission from a single crystal target occurs with non-isotropic angular and energy distributions. On our CAMECA ims 1270 ion microprobe, the secondary beam is cut by the entrance and energy slits in planes conjugate to the immersion lens crossover plane of the collection optical system (de Chambost *et al.*, 1991). Secondary-ion distributions in the crossover plane are a function of initial energy and angle of ion emission so that variations in the sputtering conditions at the sample surface (charging, development of topography, etc.) can change the density distributions of Th$^+$ and Pb$^+$ in these planes and therefore affect the relative sensitivity factor (RSF) for these species. Because sample charging and crater development are believed to be major contributors to these variations, care is taken to control the surface potential and crater depth during analysis. The depth/diameter ratios of the sputtered craters were maintained at <0·1 and monitoring of energy spectra indicates that changes in the average surface potential of the analyzed area under our measurement conditions were <1 eV. In addition, an aperture was inserted into the beam path at an image plane to reject secondary ions emitted from near the edge of the crater, where the extraction field is far from uniform. A further benefit of this optical gating is a substantial reduction of common Pb associated with surface contamination.

The energy distributions of Pb$^+$ and Th$^+$ secondary ions differ markedly, with Pb$^+$ behaving in a fashion similar to a molecular ion (Harrison *et al.*, 1995*b*). A plot of ^{264}ThO$_2$$^+$/^{232}Th$^+$ vs ^{208}Pb*$^+$/^{232}Th$^+$ for a standard monazite yields a linear array (the calibration curve) allowing the RSF to be derived by dividing the measured ^{208}Pb*$^+$/^{232}Th$^+$ of the standard at a reference ^{264}ThO$_2$$^+$/ ^{232}Th$^+$ value by its known ^{208}Pb*/^{232}Th (Fig. 4). The age of an unknown, measured under identical conditions, can then be determined by applying this RSF. For ~20 Ma monazites, the precision of the method is not limited by counting statistics but by the reproducibility of the calibration curve, which is typically ±2%. The accuracy of the method depends critically on usage of a well-characterized standard monazite.

Monazite standard 554

Our primary monazite standard is separated from sample 554, a mildly deformed peraluminous granodiorite from
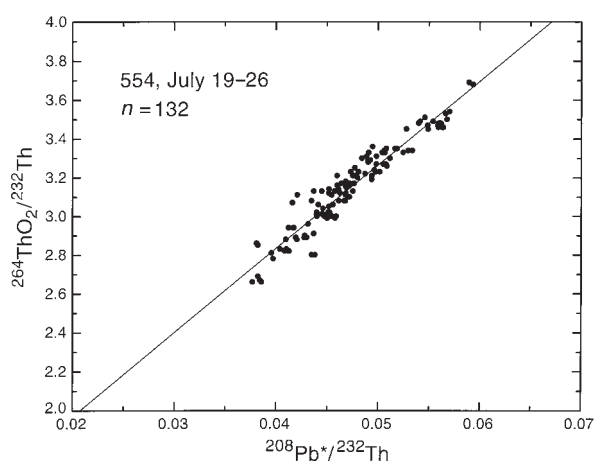
Fig. 4. A typical $^{264}\mathrm{ThO_2}^+/^{232}\mathrm{Th}^+$ vs $^{208}\mathrm{Pb}^+/^{232}\mathrm{Th}^+$ calibration curve for monazite standard 554 obtained over a period of 1 week. By using the age of 554 (45 ± 1 Ma), this relationship allows a relative sensitivity factor to be calculated, which permits determination of Pb/Th ratios of unknowns measured under the same conditions.

Whole-rock isotopic and trace element analysis

Previous work (e.g. Deniel *et al.*, 1987; Guillot, 1993) has shown that the Manaslu granite is characterized by spatial variability in trace element concentrations and isotopic compositions over multiple length scales. To relate trends observed in the Th–Pb monazite dating to key geochemical indicators, we provide several trace element and isotopic results for the whole-rock samples used in the age determinations. Guided by the earlier investigations, we chose Rb/Sr, $^{87}\mathrm{Sr}/^{86}\mathrm{Sr_i}$, and Th/U as these parameters. Whole-rock Sm–Nd and Pb isotopic results were also obtained for four samples. Data shown in bold were obtained at UCLA using the methods described by Nelson & Davidson (1993). All other isotopic results were undertaken at the University of Clermont-Ferrand and are compiled from Deniel *et al.* (1987) and Guillot (1993). U and Th were analyzed at CRPG Nancy using the methods of Govindaraju *et al.* (1976).

RESULTS
Manaslu granite

In an earlier paper we reported Th–Pb ion microprobe dating results on sample U315, located near the base of the pluton where the Chhokang Arm meets the main body of the Manaslu granite (Fig. 2). Two distinct age populations were recognized; the majority of ages defined a normal distribution with a mean age of $22\cdot4 \pm 0\cdot5$ Ma (±2 SE) that was interpreted to be the age of crystallization. A single inherited grain yielded ages of ~600 Ma (Harrison *et al.*, 1995*b*).

High-density concentrates were obtained from an additional 11 spatially separated samples (~1 kg each) of the Manaslu granite (Fig. 2) from which monazites were hand picked. Each concentrate yielded ~40–60 monazite grains of ~30–80 μm in size. Twenty grains from each sample were mounted together with the 554 standard in an epoxy disk of 1 inch diameter, ground flat using 1200 SiC grit, polished using $1-\frac{1}{4}$ μm diamond paste, cleaned, and sputter coated with ~200 Å of Au. Our initial analyses were undertaken using a 2–3 nA primary beam of O^- with a spot size of ~30 μm diameter. All monazite ages reported have been corrected for common Pb based on the average Manaslu whole-rock $^{208}\mathrm{Pb}/^{204}\mathrm{Pb}$ ratio of $39\cdot4 \pm 0\cdot1$ (Table 2; Vidal *et al.*, 1982). Results of all 186 Th–Pb age measurements are available from our web page (http://oro.ess.ucla.edu/ionprobe/manaslu.html), and are summarized in Table 1.

With the exception of XG43, all monazite samples analyzed under the analysis conditions described above yielded an early Miocene age peak with a distribution of individual ages similar in form to that previously seen for U315 (see Table 1). A substantial inherited component

the Santa Catalina Mountains, Arizona [site 82 of Force (1997)]. The separated monazite contains abundant ~0·2 mm grains that vary from inclusion rich to inclusion free. Prior U–Pb isotope dilution analyses of 554 showed that the sample is too young and U poor (~130 ppm) to yield precise $^{206}\mathrm{Pb}/^{238}\mathrm{U}$ ages (G. Gehrels & R. Parrish, personal communication, 1994). The $^{206}\mathrm{Pb}/^{238}\mathrm{U}$ ages vary between 54 and 45 Ma, whereas the mean $^{207}\mathrm{Pb}/^{235}\mathrm{U}$ age is 46 ± 1 Ma. $^{232}\mathrm{Th}–^{208}\mathrm{Pb}$ isotope dilution analyses of 11 aliquots of 554 (M. Tatsumoto, personal communication, 1995) produced, with two exceptions, radiogenic yields between 98·9 and 99·8% (assuming common $^{208}\mathrm{Pb}/^{204}\mathrm{Pb} = 39\cdot5$). The two exceptions yielded $^{208}\mathrm{Pb}/^{204}\mathrm{Pb}$ ratios consistent with common Pb. We assume that these aliquots contained grains with high densities of fluid inclusions containing high concentrations of common Pb. Omitting the lowest value (>3σ from the mean) yields an age of $45\cdot3 \pm 1\cdot4$ Ma (2σ). This error is still greater than the <2% dispersion routinely observed on calibration curves for 554 monazite (Fig. 4). This suggests that the grains selected for ion microprobe analysis are uniform in Pb/Th to at least that level. Intercalibration of Th–Pb monazite standards (Harrison *et al.*, 1995*b*; T. Ireland, personal communication 1995) yields an age for 554 of 45 ± 1 Ma, which is consistent with the isotope dilution results. A further test of the accuracy and reproducibility was undertaken using monazites that were well characterized by U–Pb measurements and could be shown by ion microprobe analyses to have concordant U–Th–Pb systems at the <1% level (Harrison *et al.*, 1995*b*). Intercalibration of five monazites yields an average dispersion of 1·4% from their known age.

Table 1: Ion microprobe Th–Pb monazite ages

Sample	x/y*	z (m)	Age (Ma, ±2 SE)†	n/no. used‡	MSWD	Inheritance
Manaslu intrusive complex						
Larkya La phase						
DK89	408·20/38·10	4400	21·9 ± 0·5	9/8	2·0	36 Ma
U315§	428·25/21·97	3878	22·4 ± 0·5	28/24	1·8	584–613 Ma
XG43	416·96/35·78	4980	22·7 ± 0·5	38/9	2·6	26–533 Ma
XG46	416·91/35·81	4980	23·6 ± 0·7	13/5	1·0	29–413 Ma
XG56	414·83/35·04	5440	23·2 ± 0·5	11/10	5·7	38 Ma
XG102	414·14/34·89	5140	24·0 ± 0·8	12/5	1·7	4@33 Ma, 99–423 Ma
XG270	420·39/30·50	4548	22·9 ± 0·5	13/10	0·4	3@31 Ma
XP130	425·36/28·19	4090	23·0 ± 0·5	10/10	7·3	none
Bimtang phase						
DK203	401·51/32·15	3665	19·3 ± 0·4	8/7	0·7	31 Ma
DK208	401·56/32·15	3365	19·6 ± 0·4	6/6	0·6	none
XG162	408·52/28·30	3385	19·3 ± 0·4	20/17	1·1	23–25 Ma
XL24	412·96/29·69	4040	19·0 ± 0·4	19/13	0·9	24–33 Ma
Dolpo-Mugu granite						
LO68	83°48′/29°07′		17·6 ± 0·3	20/20	1·0	none

*Lambert grid map reference, Geological Survey of India.
†Interpreted crystallization age based on peak of the age distribution.
‡Number of spot analyses/number used in age calculation (i.e. number of inherited grains).
§Datum from Harrison *et al.* (1995a).

was present in most of the samples with prominent ages of ~30–40 Ma and ~100–600 Ma (Table 1). Age assessment of sample XG43 was initially precluded as the dating results yielded a range of ages from 23·8 Ma to ~500 Ma without any distinctive peaks.

Of the 11 results (including U315 but excluding XG43), seven cluster at 22·9 ± 0·3 Ma and four at 19·3 ± 0·3 Ma (Table 1). The younger cluster yields a mean square weighted deviation (MSWD) of 1·4, consistent at the 2σ level with all four samples belonging to a single population. The MSWD of 3·7 for the older cluster is higher than the value of 2·4 expected at the 95% confidence level, suggesting that monazite crystallization occurred over a period of 0·6–1·2 my.

The broad distribution of ages obtained from XG43 (i.e. 23·8 to ~500 Ma) reflects the common occurrence of restitic monazite, which precludes obtaining an estimate of the timing of crystallization, although we interpret the minimum age of 23·8 ± 0·6 Ma to be an upper age limit. With the view that increasing spatial resolution might overcome this problem, we repolished the sample mount and undertook a detailed characterization of a single grain (XG43f) using an analysis spot of ~5 μm diameter. Eighteen Th–Pb analyses of this grain (Fig. 5) revealed an inherited core with ages varying from 102 to 533 Ma and a magmatic rim with

an age of 22·7 ± 0·5 Ma (Table 1), consistent with the seven other results from the central and northeastern portions of the pluton. We have previously noted (e.g. Edwards & Harrison, 1997) that the shape of restitic monazite cores inferred from ion microprobe analysis, not otherwise easily imaged by conventional methods, is substantially more irregular that that routinely observed for zircon. All eight samples in the older group (Table 1) yield a mean age of 22·9 ± 0·6 Ma, which we interpret as the crystallization interval. The $^{40}Ar/^{39}Ar$ mica ages for these older rocks average 17·6 ± 0·8 Ma, with none in excess of 18·6 Ma (Copeland *et al.*, 1990). Because no $^{40}Ar/^{39}Ar$ results exceed the interpreted Th–Pb age of the younger intrusive rocks, we infer that rocks in the older group remained at sufficient depth (>10 km; Guillot *et al.*, 1995) to remain open to argon loss or to be reset by the associated thermal pulse. It should be noted from Table 2 that this group is characterized by relatively high Rb/Sr (4–11) and $^{87}Sr/^{86}Sr_i$ (>0·752) ratios, suggestive of a derivation from a source containing a mica-rich, metapelitic component. It should be noted also, however, that the seven samples of this age group, although dominantly two-mica leucogranites, also contain tourmaline and two-mica tourmaline varieties.

The four rocks that define the 19·3 ± 0·3 Ma phase are spatially restricted to the southwestern side of the

Table 2: Whole-rock isotopic and trace element data for Manaslu granite samples used for Th–Pb geochronology

Sample	Type*	Age (Ma)	Rb (ppm)	Sr (ppm)	$^{87}Rb/^{86}Sr$	$^{87}Sr/^{86}Sr$	Th (ppm)	U (ppm)	Th/U
Larkya phase									
DK89	2M	21·9 ± 0·7	311	87·0	10·35	n.d.	n.d.	n.d.	n.d.
U315	2M	22·4 ± 0·5	**393**	**51·4**	**22·2**	**0·759326**	n.d.	n.d.	
XG43	T	22·7 ± 0·5	438	47·0	25·63	0·773818	3·40	9·88	0·34
XG46	2MT	23·6 ± 0·7	306	47·0	22·14	0·771027	2·89	11·9	0·24
XG56	2M	23·2 ± 0·5	**433**	**41·6**	**30·27**	**0·765090**	3·51	13·6	0·26
XG102	2M	24·0 ± 0·8	**470**	**44·7**	**30·55**	**0·761066**	4·85	15·9	0·31
XG270	2M	22·9 ± 0·5	349	65·0	15·55	**0·760331**	3·00	9·35	0·32
XP130	2M	23·0 ± 0·5	**369**	**49·8**	**21·52**	**0·752333**	3·00	9·35	0·32
Bimtang phase									
DK203	2M	19·3 ± 0·4	303	105	8·38	0·748998	6·50	13·8	0·47
DK208	2M	19·6 ± 0·4	316	109	8·44	0·748189	8·83	3·94	2·24
XG162	2M	19·3 ± 0·4	114	114	2·90	**0·746491**	5·17	4·82	1·07
XL24	2MT	19·0 ± 0·4	276	83·0	9·63	**0·744458**	3·57	4·81	0·74
	Sm (ppm)	Nd (ppm)	$^{147}Sm/^{144}Nd$	$^{143}Nd/^{144}Nd$	$^{208}Pb/^{204}Pb$	$^{207}Pb/^{204}Pb$	$^{206}Pb/^{204}Pb$		
XG56	**1·86**	**5·76**	**0·1967**	**0·511952**	**39·252**	**15·778**	**18·846**		
XP130	**1·69**	**5·85**	**0·1740**	**0·511912**	**39·231**	**15·779**	**18·679**		
XG102	**2·37**	**7·67**	**0·1856**	**0·511911**	**39·248**	**15·744**	**18·708**		
U315	**2·41**	**7·91**	**0·1848**	**0·511952**	**39·337**	**15·778**	**18·865**		
DK208	4·00	15·4	0·1590	0·511894	n.d.	n.d.	n.d.		

*2M, two-mica granite; T, tourmaline granite; 2MT, two-mica + tourmaline granite.
Data in bold were produced at UCLA. See section 'Whole rock isotopic and trace element analysis' for other sources.
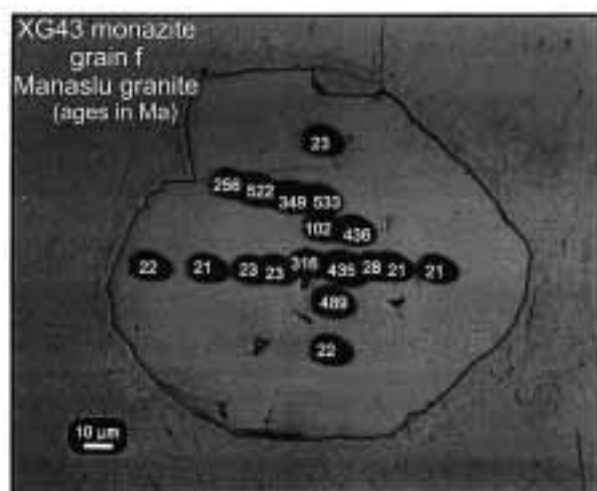

Fig. 5. Photomicrograph of XG43 grain f showing location of spot analyses together with calculated ages in Ma. Although the Au coating is removed from a larger area, the actual size of analyzed region is ~5 μm in diameter.

pluton, where Deniel *et al.* (1987) obtained an Rb–Sr whole-rock isochron relationship on a suite of fine-grained samples (Fig. 2). Recalculation of Rb/Sr data using the algorithm of Mahon (1996) yields an age of 18·3 ± 0·5 Ma. Mica $^{40}Ar/^{39}Ar$ ages are distinctly younger (15·6 ± 0·6 Ma; Copeland *et al.*, 1990) than those yielded by the older, coarser-grained leucogranite in the central and northeastern portions of the Manaslu granite and are consistent with evidence for greater emplacement depths (~20 km; Guillot *et al.*, 1995). Compared with these rocks (Fig. 2), the ~19 Ma samples have a higher average Th/U (1·1 vs 0·35), and lower Rb/Sr (1–3 vs 4–11) and $^{87}Sr/^{86}Sr_i$ (<0·749 vs >0·752) (Table 2; Guillot, 1993). If we assume that these textural and geochemical distinctions are intrinsic to the younger phase and that we can therefore use them as a basis for estimating the fraction of the exposed pluton that was emplaced at 19·6–19·0 Ma, then the ~19 Ma phase represents about one-third of the present exposure of the Manaslu granite. Although this estimate is opposite to that inferred from the bimodal distribution of $^{87}Sr/^{86}Sr_i$ ratios (Guillot & Le Fort, 1995) that are dominated by the <0·752 group, geochemical sampling coverage is biased toward the southwestern side of the pluton (Guillot, 1993). Again, we note that the four samples contain both two-mica and two-mica tourmaline

leucogranite types. Lastly, we point out that the younger phase yielded no pre-Tertiary monazite ages (Table 1), consistent with much lower levels of restitic monazite compared with the older phase. Because the parameter most sensitive to monazite dissolution is melting temperature, this probably reflects higher peak temperatures for the younger granite. However, other effects, such as a decreased water activity, or a lower abundance of restitic monazite (or a large average grain size) in the source, could also potentially influence monazite dissolution.

The evidence presented for episodic injection of discrete magmas clearly indicates that the Manaslu granite is an intrusive complex and requires us to distinguish between the two magmatic phases thus far recognized. Henceforth, we shall refer to the younger, ~19 Ma, apparently lower $^{87}Sr/^{86}Sr_i$ granitoid as the Bimtang phase, and the ~23 Ma, higher $^{87}Sr/^{86}Sr_i$ intrusion as the Larkya La phase (see Fig. 3). Because these two plutons contain a complex mixture of two-mica and tourmaline leucogranites, petrologic models emphasizing the need for contrasting physical conditions in the genesis of the different granite types appear not to be supported by our observations (Guillot & Le Fort, 1995).

Dolpo-Mugu granite

The North Himalayan granite belt runs parallel to, and ~80 km to the north of, the High Himalaya (Fig. 1). In contrast to the generally sheet-like High Himalayan leucogranites, the North Himalayan granites belt is composed of ~16 elliptical plutons totaling 4000 km^2 in area that intrude into Tethyan metasedimentary rocks (Debon *et al.*, 1986; Le Fort, 1986). They differ from the High Himalayan leucogranites in their emplacement style, younger ages (15–9 Ma), and higher melting temperatures as evidenced by noneutectic compositions, lower monazite inheritance, and a monazite saturation temperature of >760°C (Debon *et al.*, 1986; Schärer *et al.*, 1986; Montel, 1993). Their relative youth with respect to the High Himalayan leucogranites has been ascribed to a low rate of fluid infiltration (Le Fort, 1986) and thermal refraction from the Tethyan sedimentary rocks coupled with low heat production (Pinet & Jaupart, 1987).

The Dolpo-Mugu granite (Le Fort & France-Lanord, 1995) is a 1600 km^2 pluton that straddles the High and North Himalayan belts (Fig. 1). The adjacent Mustang granite appears to have been circular in cross-section before development of the Thakkhola graben, which bisected the pluton and buried its eastern half (Fig. 1). The inferred circular shape of the Mustang granite and its alignment along strike with the northerly belt (Fig. 1) distinguishes it as a North Himalayan granite. Because the Dolpo-Mugu granite straddles the region separating

the two belts and is relatively inaccessible, it is difficult to similarly characterize. We undertook Th–Pb monazite dating on a sample of the Dolpo-Mugu granite with the goal of distinguishing with which plutonic series it is most appropriately associated.

Twenty analyses of monazite separated from sample LO68 yield a single population (MSWD = 0·97) with a Th–Pb age of 17·6 ± 0·3 Ma (Table 1). Two splits of the LO68 monazite separate yield isotope dilution Th–Pb ages of 17·13 ± 0·12 and 17·77 ± 0·12 Ma (F. Oberli & M. Meier, personal communication, 1996). Although the isotope dilution ages are separated from each other at the 5σ level, their average value of 17·5 Ma is indistinguishable from the ion microprobe result of 17·6 Ma. Inheritance and/or Pb* loss could explain the difference between the isotope dilution ages, but the normal distribution and MSWD of the ion microprobe age distribution of unity tend to rule out these effects. More likely, this discordance represents a minimum crystallization interval of 0·4–0·6 m.y. It should be noted that the uncertainty on individual ion microprobe spot ages is typically ±0·5 Ma and thus our method is insufficiently precise to distinguish between a single event at 17·6 ± 0·3 Ma and a protracted magmatic history extending over 0·5 my. None the less, this result further demonstrates our ability to accurately date ~17 Ma monazites using our 45 Ma 554 monazite standard.

DISCUSSION
Manaslu granite

A plot of all 186 Th–Pb spot ages of Manaslu monazites (Fig. 6) clearly reveals two magmatic pulses at ~23 and ~19 Ma, and also shows the spectrum of ages resulting from the incorporation of restitic monazite containing inherited Pb. Interpreting this broad age spectrum in terms of protolith ages is complicated by the potential for hybrid ages to result from diffusive loss and/or overlap of the ion microprobe beam on both rim and core. None the less, we are confident in inferring the existence of at least two restitic monazite components. The clustering of ages between 30 and 40 Ma probably includes monazite formed in the Greater Himalayan Crystallines during Eo-Himalayan metamorphism (Hodges *et al.*, 1996; Le Fort, 1996; Parrish & Hodges, 1996; Edwards & Harrison, 1997). This phase of metamorphism is manifested as higher-pressure prograde assemblages in the GHC that are overprinted by Neogene metamorphism related to slip on the MCT (Pêcher, 1989). The second grouping of ages, between 450 and 600 Ma, probably reflects the effects of Pan African magmatism, which is well documented to have affected the northern margin of the Indian craton, the inferred protolith of the Himalayan gneisses (Le Fort *et al.*, 1982; Schärer & Allègre, 1983;
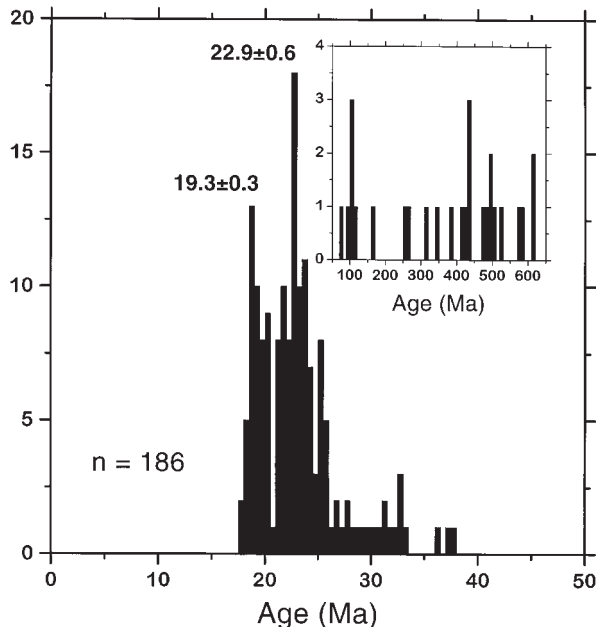
Fig. 6. Histogram of all 186 Th–Pb monazite ages from the Manaslu intrusive complex. The peaks at 23 Ma and 19 Ma correspond, respectively, to the Larkya La and Bimtang phases. The tailing to much older ages is interpreted as the result of inheritance from ~40 Ma and ~500 Ma protoliths.

Le Fort *et al.*, 1986; Copeland *et al.*, 1988; Parrish & Hodges, 1996).

Assuming that the crystallization ages given in the caption of Fig. 1 are representative of the plutons from which they were sampled, it appears that about three-quarters of the ~8000 km^2 of leucogranite exposed along the crest of the High Himalaya (Le Fort *et al.*, 1987), including the Larkya La phase of the Manaslu granite, was emplaced in the relatively brief interval between 24 and 22 Ma.

The Bimtang phase of the Manaslu granite, apparently spatially restricted to the structurally deeper, southwestern side of the intrusive complex, was emplaced at 19·3 ± 0·3 Ma, ~4 my after the Larkya La phase. A leucogranite stock intruded into the Greater Himalayan Crystallines ~30 km to the southwest of the Manaslu granite also yields ~19 Ma U–Pb monazite ages (Coleman & Parrish, 1995) and another small leucogranite body near Nyalam (Fig. 1), ~200 km to the east, yields a similar age (Schärer *et al.*, 1986). Although it is at least arguable that magmatism in the High Himalaya was dominantly bimodal in age with peaks at 23 and 19 Ma, other small bodies yield ages of ~20 and ~17 Ma (Noble & Searle, 1995; Searle *et al.*, 1997), leaving open the possibility that there may have been a continuum of magmatic activity from 24 to ~18 Ma. However, it is clear that models of High Himalayan leucogranite magmatism must account for a minimum duration of 5 my.

The behavior of monazite during anatexis is well understood in terms of its solubility in the melt (Montel, 1993). Once the melt reaches saturation, restitic monazite cores are stabilized in the melt and later provide a site for nucleation of new magmatic monazite. The kinetics of monazite dissolution suggests that crystals of ~50 μm will dissolve relatively rapidly to the point of saturation (Rapp & Watson, 1986) under conditions expected in High Himalayan leucogranite melts (i.e. ~5% H$_2$O, ~700–775°C; Scaillet *et al.*, 1995). While exposed to the melt, restitic cores passively record the duration of that interval via the diffusive loss of their Pb* to the liquid. In conjunction with accessory mineral thermometry (Harrison & Watson, 1983; Montel, 1993; Ayres *et al.*, 1997), which provides an estimate of peak melting temperature, we can use the ion microprobe to investigate the distribution of Pb* within inherited cores and recover this temporal information. Because of the high Pb* concentrations within inherited cores in these rocks, we can also utilize the U–Th–Pb systems to determine the degree of isotopic re-equilibration.

Although these calculations require some assumptions regarding the mineral dissolution history (see Watson, 1996) and assume that crystal fractionation has not occurred, a first-order estimate of the duration spent at peak temperature, t, can be obtained using the simple relationship $t = x^2/(D_o \, e^{-E/RT})$, where x represents the maximum length scale of diffusive exchange, estimated from Fig. 5 to be 5 μm, $E = 43$ kcal/mol, and $D_o = 7 \times 10^{-11}$ cm^2/s (Smith & Giletti, 1997). Taking the peak temperature estimated for the Larkya La phase from zircon and monazite saturation thermometry of ~750°C, a monazite–melt interface would produce a surface depletion layer of Pb* with a characteristic length of 5 μm in 0·2 my, with an associated uncertainty of an order of magnitude. With the caveats mentioned above, we conclude that the maximum duration between the melting of the XG43 source rock and emplacement of the magma into the Manaslu pluton was <2 my.

The Th–Pb ion microprobe results presented here appear to resolve the three questions raised in the 'Prior age constraints' section with regard to our earlier, solitary result. The Manaslu intrusive complex is heterogeneous with respect to age at the >1 my level, with two phases of intrusion identified at 22·9 ± 0·6 Ma and 19·3 ± 0·3 Ma. The persistence of the ~500 Ma protolith ages in samples with demonstrable ~23 Ma magmatic rims effectively rules out sample contamination as the source of this component. This same grain rim–core age relationship also tends to rule out the possibility that the ~23 Ma ages reflect metamorphic recrystallization. However, monazite that pre-dates magmatism by ~10–15 my is recognized and appears to be related to prograde crystallization of monazite during the Eo-Himalayan phase of collision (Le Fort, 1996).

Dolpo-Mugu granite

Crystallization between 17·9 and 17·1 Ma places this granite at the upper end of the range of $^{207}Pb/^{235}U$ monazite ages previously determined for North Himalayan granites by Schärer *et al.* (1986), but below the lower bound for the voluminous High Himalayan leucogranites (Harrison *et al.*, 1997a). Although its structural location, age, and apparent lack of inheritance suggest that the Dolpo-Mugu granite is more akin to that belt than the High Himalayan chain (Harrison *et al.*, 1997a), two issues raised by the present study condition that conclusion. The Dolpo-Mugu granite is one of the largest Tertiary plutons of the Himalayan range (Fig. 1) and, as we have found in the case of the Manaslu massif, one sample is insufficient to characterize a large body. Our results also raise the question of whether Himalayan granitoid magmatism is confined to two separate belts or is in fact a spatiotemporal continuum produced by progressive dehydration melting (Harrison *et al.*, 1999).

Implications for the timing of deformation

Because the Manaslu intrusive complex crosscuts extensional structures in the hanging wall of the detachment, we infer that these features must be older than 19–23 Ma. The phase of syn-magmatic oblique-slip normal shearing within the Larkya La phase must have been active between 23·5 and 22·3 Ma. However, leucogranite dikes observed to crosscut the detachment immediately beneath the southeastern side of the pluton have not been dated.

U–Th–Pb monazite dating of other leucogranite bodies indicates a protracted slip history for the STDS throughout the Himalaya. In the western Himalaya, a small leucogranite in the Zanskar region beneath (and not cut by) the STDS yields an age of 19 $\pm$ 1 Ma (Noble & Searle, 1995). Footwall $^{40}Ar/^{39}Ar$ cooling ages between 18 and 15 Ma (T. M. Harrison, unpublished data, 1997) suggest that activity on the basal detachment was probably limited to the interval 20–17 Ma. Near Shisha Pangma, Searle *et al.* (1997) concluded that the age of normal faulting must largely post-date a leucogranite body dated at 17·3 $\pm$ 0·3 Ma. Lastly, in the eastern Himalaya (Fig. 1), the detachment remained active until at least 12·5 $\pm$ 0·4 Ma (Edwards & Harrison, 1997).

There are at least three possible explanations for this apparent diachroneity (see Edwards & Harrison, 1997). The first is that the STDS represents a single, northward propagating normal fault system, in which case the variations in age along strike are due to the rollback of the location of the basal detachment. Second, a topographic gradient capable of driving an STDS-type normal fault system may have initiated much later in the eastern Himalaya relative to locations further west. Third, the

north-directed thrusts in southeastern Tibet (the Renbu Zedong Thrust System; Quidelleur *et al.*, 1997) may have accommodated STDS displacement in the eastern Himalaya much later than in the western Himalaya.

A mechanism for diachronous leucogranite production from a single source region

Our results present a new challenge to the problem of leucogranite magma genesis. Specifically, how can hundred-km^2-sized bodies that differ in age by 4 my be generated from the same crustal source region during continental collision? Below we evaluate whether available models are individually capable, or able when acting in concert, to explain this phenomenon. Our criteria to judge the success of each model in the present context are its ability to predict (1) the emplacement of juxtaposed granite plutons of ~200 km^2 separated in emplacement age by 4 my, and (2) a decrease in $^{87}Sr/^{86}Sr_i$ and Rb/Sr, and concomitant increase in melting temperature for the younger phase relative to that of the older leucogranite.

Le Fort (1975) proposed that fluids introduced into the GHC from the dehydrating footwall following nappe emplacement fluxed the gneisses to produce the High Himalayan leucogranite melts via minimum melting reactions. Alternatively, Harris *et al.* (1993) proposed that the leucogranites were produced by higher-temperature, muscovite dehydration melting (e.g. Thompson, 1982) and became mobile only after tectonic decompression (via the STDS) markedly increased the melt fraction. The high Rb/Sr ratios observed in the Himalayan leucogranites seem to preclude the former and heavily favor dehydration melting. Specifically, measured leucogranite Rb/Sr values are typically 2–6 whereas those determined for the GHC source rocks lie in the range 0·7–1·4 (Vidal *et al.*, 1982; Harris *et al.*, 1993). Because the relative proportion of mica (the principal host of Rb in the protolith) to feldspar (the main repository for Sr) consumed in water-saturated melting is small, Rb/Sr ratios are not enriched in minimum melts. Conversely, as breakdown of mica during dehydration melting preferentially releases Rb with respect to Sr, this mechanism has the potential to produce the high Rb/Sr ratios observed for the leucogranites. Furthermore, recent experimental evidence indicates that water-saturated melting of Himalayan source rocks produces melt of trondhjemitic rather than leucogranitic composition (Patiño Douce & Harris, 1998).

Although such arguments make it seem probable to us that dehydration melting was responsible for Himalayan anatexis, we consider it unlikely that both melting episodes were triggered by tectonic decompression. First, to induce even one melting event requires very high and
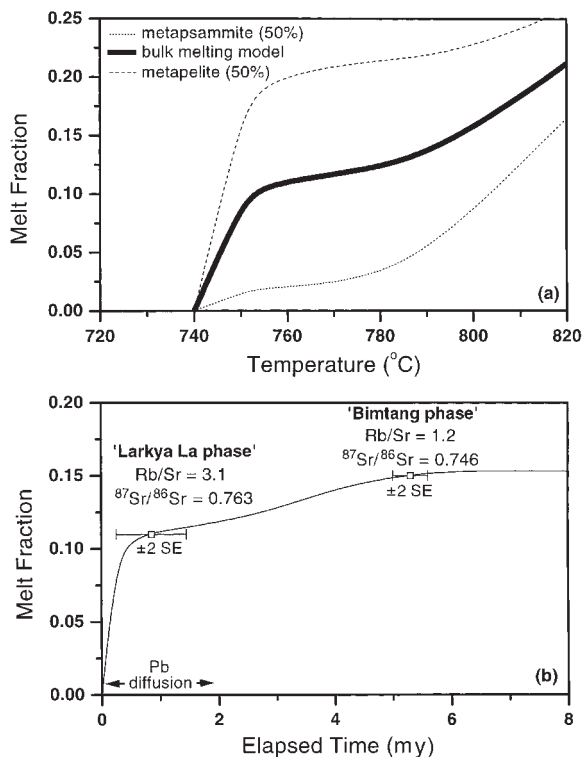
Fig. 7. (a) Melting relationships of intercalated pelitic and psammitic source rocks used in calculations. The bold curve represents the bulk melting properties derived from melting of a source containing equal quantities of metapelite (long-dashed line) and metapsammite (short-dashed line). (b) Calculated melt fraction in the source region as a function of time since initiation of thrusting. The position of the source region is initially 230 km from the left edge of the numerical grid used by Harrison *et al.* (1999). The positions on the curves corresponding to the two melting pulses at 11% and 15% total melting are indicated as 'Larkya La phase' and Bimtang phase', respectively. The associated error bars reflect the ±2 SE uncertainty on the ages determined in this study. It should be noted that the contrast in age between the two melting peaks of ~4 my is the same as the difference between emplacement of the Larkya La (22·9 $\pm$ 0·6 Ma) and Bimtang (19·3 $\pm$ 0·3 Ma) phases. The duration of the melting event leading to emplacement of the Larkya La phase, estimated from consideration of the length scale of Pb diffusion in a restitic monazite core, is indicated.

sustained denudation rates. For example, the melting model of Harris & Massey (1994) requires >25 km of denudation to produce 8% melting because of decompression, a value which exceeds the maximum structural thickness of the Greater Himalayan Crystallines (e.g. Hodges *et al.*, 1988*b*). Although other melting models (e.g. Gardien *et al.*, 1995; Fig. 7a) require less exhumation to achieve a similar effect, the issue remains as to whether this effect is capable of generating two magmatic pulses separated temporally by 4 my. We return to this question later, but conclude that tectonic decompression by itself is not a viable mechanism.

A number of models have linked granite formation to shear heating along the Himalayan thrust system (e.g. Le Fort, 1975; England *et al.*, 1992). Recently, Harrison

et al. (1997*a*, 1999) suggested that the origin of both the High and North Himalayan granite belts could be linked to shear heating on a continuously active décollement that cuts through Indian supracrustal rocks that were transformed into basement during the initial stages of the Indo-Asian collision. Harrison *et al.* (1999) approximated the deformation history of the Himalaya and then calculated the distribution of melting that would result from shear heating along the MCT décollement. Assuming a melting relationship that yields pulses of magma at temperatures of 740–750°C and >780°C (Fig. 7a), they found that two temporally distinct granite belts separated by ~80 km (corresponding to the High and North Himalayan chains) could form from shear stresses along the thrust as low as 20–30 MPa. Although High Himalayan leucogranite anatexis as a result of muscovite dehydration melting along the décollement was largely confined to a ~2 my interval in this model, Harrison *et al.* (1999) demonstrated that an increase in shear stress from 30 MPa to 50 MPa would result in additional, delayed melting from the same source region. Below we explore the extent to which the progressive melting model of Harrison *et al.* (1999) is capable of explaining the geochemical characteristics of the temporally distinct magmatic phases within the Manaslu intrusive complex.

Harrison *et al.* (1999) represented the integrated melting properties of the source region by averaging experimentally determined melting relationships for various metasedimentary bulk compositions (Gardien *et al.*, 1995). In the present discussion, we can consider the melt fraction vs temperature relationship as representing the contributions of two sub-equal interlayered components in the GHC source region: muscovite-rich, plagioclase-poor pelitic gneisses and muscovite-poor, plagioclase-rich psammitic rocks (Table 3). The relationships between melt fraction and temperature appropriate for each of these bulk compositions, based upon muscovite and biotite dehydration melting (Le Breton & Thompson, 1988; Gardien *et al.*, 1995), are shown in Fig. 7a. It should be noted that the extent of lower-temperature melting (740–755°C) in each of the lithologies is dictated by muscovite abundance whereas biotite dehydration melting (>785°C) in the metapelite is limited by the complete consumption of plagioclase at higher temperature. Although certain lithologies present in the GHC will be more refractory to melting than indicated by these curves (e.g. Patiño Douce & Harris, 1998), we can rule out candidate source rocks that require melting temperatures >800°C (Montel, 1993).

Following the approach of Harrison *et al.* (1999), but assuming a 50% higher shear stress of 45 MPa, we calculated the melt fraction as a function of time for a given source region position (Fig. 7b). Although the higher shear stress could reflect the dehydration of the

Table 3: Trace element partitioning and isotopic variation during batch melting

Mineral	Unmelted source		Residual solid		Integrated	Residual solid		Integrated
	Pelite	Psammite	Pelite	Psammite	Melt 1*	Pelite	Psammite	Melt 2†
Quartz	27	31	21	30		26	29	
Plagioclase	6	10	1	9		0	7	
K-feldspar	0	20	12	21		15	22	
Muscovite	32	3	0	0		0	0	
Biotite	10	30	10	30		11	27	
Garnet	20	6	20	6		26	8	
Sillimanite	5	0	16	1		20	1	
Melt	0	0	20	2		2	6	
Total	100	100	100	100		100	100	
Rb	109	81	182	73	172	191	81	106
Sr	75	254	52	97	57	53	268	88
Rb/Sr	1·1	0·32	3·5	0·75	3·0	3·6	0·30	1·2
$^{87}Sr/^{86}Se$	0·765	0·740	0·765	0·740	0·763	0·765	0·740	0·746

*Residual bulk partition coefficients: pelite Rb 0·50, Sr 1·53; psammite Rb 1·12, Sr 2·64.
†Residual bulk partition coefficients: pelite Rb 0·46, Sr 1·52; psammite Rb 1·05, Sr 2·68.

thrust surface following the initial phase of melting, variations of other melting parameters [see fig. 7 of Harrison *et al.* (1999)] could produce the required melting with a lower shear stress. Although we will later conclude that decompression alone cannot trigger the two episodes of leucogranite magmatism, this mechanism could work in concert with frictional heating to reduce the required flow stress to a few hundred bars, which we have previously argued could be maintained along a thrust surface at ~750°C (Harrison *et al.*, 1997*a*). We also note that because both phases of the Manaslu intrusive complex are emplaced within the hanging wall of the STDS, the source of the ~19 Ma magmatic pulse could be significantly further north within the GHC than the ~23 Ma phase. The higher temperatures further down dip along the MCT would be conducive to the second melting episode appearing earlier than our model predictions and thus be consistent with a lower shear stress.

Coupled to the melting relationship (Fig. 7a), our thermal model predicts that ~11% melt is generated from the heat produced during the initial 1–2 my of slip along the décollement, and an additional 4% is produced after 4–5 my (Fig. 7b). It should be noted that the intervening ~4 my between the initial melting pulse and higher-temperature anatexis is comparable with the interval between emplacement of the Larkya La and Bimtang phases. In addition, the fraction of lower-temperature melt exceeds that produced at higher temperature by a factor of two to three, similar to the inferred proportions of the ~23 Ma and ~19 Ma leucogranite

phases. Dropping the flow stress by a factor of two significantly increases the time before appearance of the second melt phase.

Assuming that the leucogranite source region can be characterized by the present exposure of Formation I within the GHC (Guillot & Le Fort, 1995), the melting history (Fig. 7) can be used to predict the trace element and isotope geochemistry of the Manaslu magmas. Rb/Sr and $^{87}Sr/^{86}Sr_i$ correlate well with bulk composition in these rocks (Guillot & Le Fort, 1995). On the basis of the data of Vidal *et al.* (1982) and Deniel *et al.* (1987), we characterize the metapelites as having Rb/Sr = 2 and $^{87}Sr/^{86}Sr$ = 0·765 and the metapsammitic rocks by Rb/Sr = 0·8 and $^{87}Sr/^{86}Sr$ = 0·740 (Table 3). Experimentally determined diffusion properties of Sr (e.g. Cherniak & Watson, 1992) of the constituent phases in the >700°C source region lead us to assume that all phases within a given compositional band are equilibrated with respect to $^{87}Sr/^{86}Sr$ at the time of anatexis. Using the expression for element partitioning during batch melting together with trace element partition coefficients (Henderson, 1982; Nash & Crecraft, 1985; Harris *et al.*, 1995) yields $^{87}Sr/^{86}Sr_i$ = 0·763 and Rb/Sr = 3 for the initial phase of 11% melting (Fig. 7 and Table 3) and $^{87}Sr/^{86}Sr_i$ = 0·746 and Rb/Sr = 1·2 for the second, higher-temperature episode that produced an additional 4% melt (Fig. 7 and Table 3). The modal changes during partial melting are dictated by the stoichiometry of reactions specified by equations (2) and (3) of Harris *et al.* (1995), and the melt contributions from the intercalated

pelitic and psammitic sources are integrated to yield the above values (see Table 3). The values of $^{87}Sr/^{86}Sr$ predicted by the above calculations agree well with the bimodal distribution observed in the Manaslu complex (Guillot & Le Fort, 1995). Although the calculated values of Rb/Sr are at the lower end of those observed (Guillot & Le Fort, 1995), use of a continuous extraction melting model and different parameters (relative abundance of phases, melt fraction, partition coefficients) can easily generate the range of observed values (see Harris et al., 1993).

The progressive melting model accounts for the $^{87}Sr/^{86}Sr_i$ and Rb/Sr systematics of the two intrusive phases, the contrast in emplacement ages, and potentially explains the observed lack of pre-Tertiary monazite inheritance in the Bimtang phase (Table 1) by virtue of its higher-temperature genesis.

Viability of decompression melting for diachronous magmatism

Recognition that most Himalayan anatexis occurred by dehydration melting reactions (e.g. Harris & Inger, 1992) stimulated increasing support for the view that melting was induced by decompression via slip along STDS (e.g. Harris et al., 1993; Harris & Massey, 1994; Guillot & Le Fort, 1995; Searle et al., 1997). Although this enthusiasm is understandable given the positive dP/dT of vapor-absent equilibria, particularly for reactions involving muscovite, the physical viability of this mechanism has not been directly addressed. Data which document diachronous anatexis (Searle et al., 1997; this study) place more specific tectono-thermal requirements upon decompression melting as an explanation for Himalayan anatexis.

To address the feasibility of decompression melting to produce diachronous anatexis, we have undertaken numerical simulations of tectonic denudation owing to extensional faulting. Using the thermal model of Harrison et al. (1995a), P–T–t paths for footwall source regions at differing horizontal distances from a normal fault dipping at 30° were calculated (Fig. 8). Although the present observed dip of the STD is much shallower (Burchfiel et al., 1992), it is unlikely that slip occurred at dip angles much lower than 30° (e.g. Jackson & McKenzie, 1983), and shallower inclinations would require sustained slip rates that are much higher than the total present convergence across the Himalaya (Bilham et al., 1997). To facilitate comparison with the shear-heating model just presented, we used an identical geothermal structure, monitored samples originating from the same initial depth of 35 km (i.e. 10 kbar), and interpret results based upon the same melting model (Fig. 7a). Calculated trajectories of footwall positions at differing distances from the normal
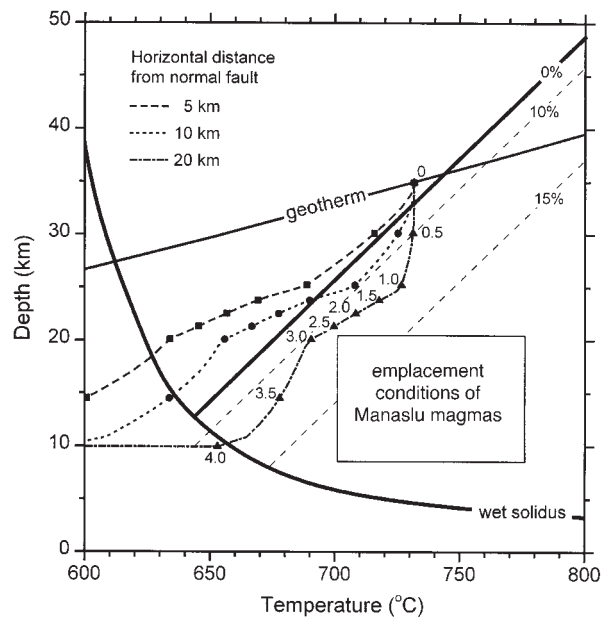

Fig. 8. Pressure–temperature diagram showing calculated trajectories of footwall positions at differing distances from a normal fault dipping at 30° (see Harrison et al., 1995a). Melting conditions shown are: wet melting of metapelites, Le Breton & Thompson (1988); muscovite–quartz–albite vapor-absent melting, Petö (1976). Emplacement conditions of the Manaslu magmas are from Scaillet et al. (1995) and Guillot et al. (1995). Vertical component of slip for footwall positions for the various time intervals are: 10 mm/yr, 2·5 mm/yr, and 10 mm/yr for 0–1 my (i.e. 24–23 Ma), 1–3 my (i.e. 23–21 Ma), and 3–4 my (i.e. 21–20 Ma), respectively. Numbers adjacent to the 20 km result are in millions of years and apply to all three curves.

fault are shown on a pressure–temperature diagram in Fig. 8 assuming a vertical component of slip of 10 mm/yr, 2·5 mm/yr, and 10 mm/yr for the time intervals 0–1 my (24–23 Ma), 1–3 my (23–21 Ma), and 3–4 my (21–20 Ma), respectively. From these starting conditions, a 10% initial melt can be obtained for source regions located >10 km from the fault given a slip rate of 20 mm/yr (corresponding to 10 mm/yr vertical component). Lower slip rates or positions closer to the normal fault result in source rocks cooling below anatetic conditions (Fig. 8). From inspection of Fig. 8, the magnitude and rate of exhaustion required to obtain two temporally distinct phases of melting seems prohibitive to us. For example, the history shown by the dot–dashed curve in Fig. 8 just succeeds in producing 1% additional melting. Higher degrees of melting would require even more rapid denudation rates than those used here. Moreover, we note that this history does not lead to anatectic or emplacement conditions consistent with those documented for the Manaslu intrusive complex (Copeland et al., 1990; Guillot et al., 1995; Scaillet et al., 1995; see box in Fig. 8).

Although we have chosen to illustrate the viability of decompression melting using the same geothermal structure as that used for the shear heating model, use

of a significantly lower geotherm (e.g. Harris & Massey, 1994) together with higher slip rates (>20 mm/yr) and total magnitude of denudation (>30 km) could produce better agreement with the known emplacement conditions of the Manaslu intrusive complex (Fig. 8). Despite our reservations regarding the viability of decompression melting, the two models make significantly different, testable predictions that should permit a clear selection between them. For example, a fundamental consequence of the decompression model is that melting occurs at progressively lower pressures and temperatures. In contrast, shear heating along a sub-horizontal décollement results in progressively higher temperature melting. Our inferences from accessory mineral saturation levels and inheritance patterns that the Bimtang phase achieved higher peak temperatures relative to those of the Larkya La phase argues against decompression melting acting alone. Finally, we wish to emphasize that the magnitude of melting from extraordinary decompression (>20–30 km) is matched by only ~40 km of sub-horizontal displacements along the basal décollement assuming modest (<50 MPa) shear stress.

source region that produced the earlier magma. Thermo-kinematic modeling indicates that: (1) two phases of leucogranite magmatism separated by ~4 my can be produced by shear heating along the Himalayan décollement assuming a shear stress of 45 MPa, and (2) scenarios involving only decompression to achieve the same result appear to require extreme conditions not permitted by available geological constraints.

CONCLUSIONS

Th–Pb monazite ages determined by the ion microprobe technique on 12 samples from the Manaslu intrusive complex are consistent with two episodes of intrusion at $22 \cdot 9 \pm 0 \cdot 6$ Ma (the Larkya La phase) and $19 \cdot 3 \pm 0 \cdot 3$ Ma (the Bimtang phase). Correlated textural and geochemical relationships suggest that the Bimtang phase represents about one-third of the present leucogranite exposure. Because the Manaslu intrusive complex crosscuts a collapse structure in the hanging wall of a detachment immediately beneath the pluton, this tectonic feature must be older than ~23 Ma. The associated synmagmatic extensional deformation within the Larkya La phase must have occurred between $23 \cdot 5$ and $22 \cdot 3$ Ma. Inherited monazite is observed in 10 of the 12 samples, with Th–Pb ages interpreted to reflect contamination by both Eo-Himalayan (~45 Ma) and Pan-African (~500 Ma) components. The scale of isotopic disequilibrium preserved within restitic monazites indicates that the Larkya La phase was at magmatic temperatures for <2 my. Dating results for a single sample from the nearby Dolpo-Mugu granite yield an age of $17 \cdot 6 \pm 0 \cdot 3$ Ma, but suggest a protracted magmatic history extending over $0 \cdot 5$ my that cannot at this time be related to the Manaslu intrusive complex.

The episode of anatexis at ~23 Ma appears to have resulted from vapor-absent muscovite dehydration melting of the Greater Himalayan Crystalline (GHC) whereas the magmatic pulse at $19 \cdot 3$ Ma is interpreted to result from higher-temperature dehydration melting of the same

REFERENCES

Ayres, M., Harris, N. & Vance, D. (1997). Possible constraints on anatectic melt residence times from accessory mineral dissolution rates: an example from Himalayan leucogranites. *Mineralogical Magazine* **61,** 29–36.

Barbey, P., Brouand, M., LeFort, P. & Pêcher, A. (1996). Granite–migmatite genetic link: the example of the Manaslu granite and Tibetan Slab migmatites in central Nepal. *Lithos* **38,** 63–79.

Bilham, R., Larson, K., Freymueller, J. & Project Idylhim members (1997). GPS measurements of present-day convergence across the Nepal Himalaya. *Nature* **386,** 61–64.

Burchfiel, B. C. & Royden, L. H. (1985). North–south extension within the convergent Himalayan region. *Geology* **13,** 679–682.

Burchfiel, B. C., Chen, Z., Hodges, K. V., Liu, Y., Royden, L. H., Deng, C. & Xu, J. (1992). The South Tibetan Detachment System, Himalayan Orogen: extension contemporaneous with and parallel to shortening in a collisional mountain belt. *Geological Society of America Special Paper* **269,** 41 pp.

Burg, J. P., Brunel, M., Gapais, D., Chen, G. M. & Liu, G. H. (1984). Deformation of leucogranites of the crystalline Main Central Sheet in southern Tibet (China). *Journal of Structural Geology* **6,** 535–542.

Chen, C. H., DePaolo, D. J. & Lan, C. Y. (1994). Rb–Sr microchrons in the Manaslu Granite: implications for Himalayan thermochronology. *Bulletin of the Institute of Earth Sciences, Academia Sinica* **14,** 44–52.

Chen, C. H., DePaolo, D. J. & Lan, C. Y. (1996). Rb–Sr microchrons in the Manaslu Granite: implications for Himalayan thermochronology. *Earth and Planetary Science Letters* **143,** 125–135.

Cherniak, D. J. & Watson, E. B. (1992). A study of Sr diffusion in K-feldspar, Na–K feldspar and anorthite using Rutherford backscattering spectroscopy. *Earth and Planetary Science Letters* **113,** 411–425.

Coleman, M. E. & Parrish, R. R. (1995). Constraints on Miocene high-temperature deformation and anatexis within the Greater Himalaya from U–Pb geochronology. *EOS Transactions, American Geophysical Union* **76,** F708.

Copeland, P., Parrish, R. R. & Harrison, T. M. (1988). Identification of inherited radiogenic Pb in monazite and its implications for U–Pb systematics. *Nature* **333,** 760–763.

Copeland, P., Harrison, T. M. & Le Fort, P. (1990). Age and cooling history of the Manaslu granite: implications for Himalayan tectonics. *Journal of Volcanology and Geothermal Research* **44,** 33–50.

Debon, F., Le Fort, P., Sheppard, S. M. F. & Sonet, J. (1986). The four plutonic belts of the Transhimalaya–Himalaya: a chemical, mineralogical, isotopic, and chronological synthesis along a Tibet–Nepal section. *Journal of Petrology* **21,** 219–250.

de Chambost, E., Hillion, F., Rasser, B. & Migeon, H. N. (1991). The CAMECA ims 1270: a description of the secondary ion optical system. In: Benninghoven, A., Janssen, K. T. F., Tumpner, J. & Werner, H. W. (eds) *SIMS VIII Proceedings.* New York: John Wiley, pp. 207–210.

Deniel, C., Vidal, P., Fernandez, A., Le Fort, P. & Peucat, J. J. (1987). Isotopic study of the Manaslu granite (Himalaya, Nepal): inferences on the age and source of the Himalayan leucogranites. *Contributions to Mineralogy and Petrology* **96,** 78–92.

Edwards, M. A. & Harrison, T. M. (1997). When did the roof collapse? Late Miocene N–S extension in the High Himalaya revealed by Th–Pb monazite dating of the Khula Kangri granite. *Geology* **25,** 543–546.

England, P., Le Fort, P., Molnar, P. & Pêcher, A. (1992). Heat sources for Tertiary metamorphism and anatexis in the Annapurna–Manaslu region, Central Nepal. *Journal of Geophysical Research* **97,** 2107–2128.

Force, E. R. (1997). Geology and mineral resources of the Santa Catalina Mountains, Southeastern Arizona. *Monographs in Mineral Science 1.* Tucson, AZ: Center for Mineral Resources, pp. 1–135.

France-Lanord, C. & Le Fort, P. (1988). Crustal melting and granite genesis during the Himalayan collision orogenesis. *Transactions of the Royal Society of Edinburgh* **79,** 183–196.

France-Lanord, C., Sheppard, S. M. & Le Fort, P. (1988). Hydrogen and oxygen isotope variations in the High Himalaya peraluminous Manaslu leucogranite: evidence for heterogeneous sedimentary source. *Geochimica et Cosmochimica Acta* **52,** 513–526.

Gardien, V., Thompson, A. B., Grujic, D. & Ulmer, P. (1995). Experimental melting of biotite + plagioclase ± muscovite assemblages and implications for crustal melting. *Journal of Geophysical Research* **100,** 15581–15591.

Govindaraju, K., Mevelle, G. & Chouard, C. (1976). Automated optical emission spectrochemical bulk chemical analysis of silicate rocks with microwave plasma excitation. *Analytical Chemistry* **48,** 1325–1331.

Guillot, S. (1993). Le granite du Manaslu (Nepal Central) marqueur de la subduction et de l'extension intracontinentales Himalayennes. *Géologie Alpine* **19,** 1–97.

Guillot, S. & Le Fort, P. (1995). Geochemical constraints on the bimodal origin of High Himalayan leucogranites. *Lithos* **35,** 221–234.

Guillot, S., Pêcher, A., Rochette, P. & Le Fort, P. (1993). The emplacement of the Manaslu granite of central Nepal: field and magnetic susceptibility constraints. In: Searle, M. P. & Treloar, P. J. (eds) *Himalayan Tectonics. Geological Society, London, Special Publication* **74,** 413–428.

Guillot, S., Hodges, K. V., Le Fort, P. & Pêcher, A. (1994). New constraints on the age of the Manaslu leucogranite: evidence for episodic tectonic denudation in the central Himalaya. *Geology* **22,** 559–562.

Guillot, S., Le Fort, P., Pêcher, A., Barman, M. R. & Aprahamian, J. (1995). Contact metamorphism and depth of emplacement of the Manaslu granite (central Nepal). Implications for Himalayan orogenesis. *Tectonophysics* **241,** 99–119.

Harris, N. & Inger, S. (1992). Trace element modelling of pelite derived granites. *Contributions to Mineralogy and Petrology* **110,** 45–56.

Harris, N. & Massey, J. (1994). Decompression and anatexis of Himalayan metapelites. *Tectonics* **13,** 1537–1546.

Harris, N., Inger, S. & Massey, J. (1993). The role of fluids in the formation of High Himalayan leucogranites. In: Searle, M. P. & Treloar, P. J. (eds) *Himalayan Tectonics. Geological Society, London, Special Publication* **74,** 391–400.

Harris, N., Ayers, M. & Massey, J. (1995). Geochemistry of granitic melts produced during incongruent melting of muscovite: implications for the extraction of Himalayan leucogranite magmas. *Journal of Geophysical Research* **100,** 15767–15777.

Harrison, T. M. & Mahon, K. I. (1995). New constraints on the age of the Manaslu leucogranite: evidence for episodic tectonic denudation in the central Himalaya—Comment. *Geology* **23,** 478–479.

Harrison, T. M. & Watson, E. B. (1983). Kinetics of zircon dissolution and zirconium diffusion in granitic melts of variable water content. *Contributions to Mineralogy and Petrology* **84,** 66–72.

Harrison, T. M., Copeland, P., Kidd, W. S. F. & Lovera, O. M. (1995a). Activation of the Nyainqentanghla Shear Zone: implications for uplift of the southern Tibetan Plateau. *Tectonics* **14,** 658–676.

Harrison, T. M., McKeegan, K. D. & Le Fort, P. (1995b). Detection of inherited monazite in the Manaslu leucogranite by ^{208}Pb/^{232}Th ion microprobe dating: crystallization age and tectonic significance. *Earth and Planetary Science Letters* **133,** 271–282.

Harrison, T. M., Lovera, O. M. & Grove, M. (1997a). New insights into the origin of two contrasting Himalayan granite belts. *Geology* **25,** 899–902.

Harrison, T. M., Ryerson, F. J., Le Fort, P., Yin, A., Lovera, O. M. & Catlos, E. J. (1997b). A late Miocene–Pliocene origin for the Central Himalayan inverted metamorphism. *Earth and Planetary Science Letters* **146,** E1–E8.

Harrison, T. M., Grove, M., Lovera, O. M. & Catlos, E. J. (1999). A unified model for the origin of Himalayan anatexis and inverted metamorphism, Main Central Thrust, Nepal Himalaya. *Journal of Geophysical Research*, in press.

Henderson, P. (1982). *Inorganic Geochemistry*. Oxford: Pergamon Press.

Hodges, K. V., Hubbard, M. S. & Silverburg, D. S. (1988a). Metamorphic constraints on the thermal evolution of the central Himalaya. *Philosophical Transactions of the Royal Society of London, Series A* **326,** 257–280.

Hodges, K. V., Le Fort, P. & Pêcher, A. (1988b). Possible thermal buffering by crustal anatexis in collisional orogens: thermobarometric evidence from the Nepalese Himalaya. *Geology* **16,** 707–710.

Hodges, K. V., Parrish, R. R. & Searle, M. P. (1996). Tectonic evolution of the central Annapurna Range, Nepalese Himalayas. *Tectonics* **15,** 1264–1291.

Jackson, J. & McKenzie, D. (1983). The geometrical evolution of normal fault systems. *Journal of Structural Geology* **5,** 471–482.

Le Breton, N. & Thompson, A. B. (1988). Fluid-absent (dehydration) melting of biotite in metapelites in the early stages of crustal anatexis. *Contributions to Mineralogy and Petrology* **99,** 226–237.

Le Fort, P. (1975). Himalayas, the collided range. Present knowledge of the continental arc. *American Journal of Science* **275A,** 1–44.

Le Fort, P. (1981). Manaslu leucogranite: a collision signature of the Himalaya, a model for its genesis and emplacement. *Journal of Geophysical Research* **86,** 10545–10568.

Le Fort, P. (1986). Metamorphism and magmatism during the Himalayan collision. In: Coward, M. P. & Ries, A. C. (eds) *Collision Tectonics. Geological Society, London, Special Publication* **19,** 159–172.

Le Fort, P. (1988). Granites in the tectonic evolution of the Himalaya, Karakoram and southern Tibet. *Philosophical Transactions of the Royal Society of London, Series A* **326,** 281–299.

Le Fort, P. (1996). The Himalayan evolution. In: Yin, A. & Harrison, T. M. (eds) *The Tectonics of Asia.* New York: Cambridge University Press, pp. 95–109.

Le Fort, P. & France-Lanord, C. (1995). Granites from Mustang and surrounding regions (central Nepal). *Journal of the Nepal Geological Society* **11,** 53–57.

Le Fort, P., Pêcher, A. & Vidal, P. (1982). Les gneiss oeillés de la Dalle du Tibet: un épisode magmatique au Paléozoïque inférieur en Himalaya du Népal. 9e Réunion Ann. Sci. Terre, Paris.

Le Fort, P., Debon, F., Pêcher A., Sonet, J. & Vidal, P. (1986). The 500 Ma magmatic event in Alpine southern Asia, a thermal episode at Gondwana scale. *Sciences de la Terre* **47,** 191–209.

Le Fort, P., Cuney, M., Deniel, C., France-Lanord, C., Sheppard, S. M. F., Upreti, B. N. & Vidal, P. (1987). Crustal generation of the Himalayan leucogranites. *Tectonophysics* **134,** 39–57.

Mahon, K. I. (1996). The New 'York' regression: application of an improved statistical method to geochemistry. *International Geological Review* **38,** 293–303.

Montel, J.-M. (1993). A model for monazite/melt equilibrium and application to the generation of granitic magmas. *Chemical Geology* **119,** 127–146.

Nash, W. P. & Crecraft, H. R. (1985). Partition coefficients for trace elements in silicic magmas. *Geochimica et Cosmochimica Acta* **49,** 2309–2322.

Nelson, S. T. & Davidson, J. D. (1993). Interactions between mantle-derived magmas and mafic crust, Henry Mountains, Utah. *Journal of Geophysical Research* **98,** 1837–1852.

Noble, S. R. & Searle, M. P. (1995). Age of crustal melting and leucogranite formation from U–Pb zircon and monazite dating in the western Himalaya, Zanskar, India. *Geology* **23,** 1135–1138.

Parrish, R. R. & Hodges, K. V. (1996). Isotopic constraints on the age and provenance of the Lesser and Greater Himalayan sequences, Nepalese Himalaya. *Geological Society of American Bulletin* **108,** 904–911.

Patiño Douce, A. & Harris, N. (1998). Experimental constraints on Himalayan anatexis. *Journal of Petrology* **39,** 689–710.

Pêcher, A. (1989). The metamorphism in the central Himalaya. *Journal of Metamorphic Petrology* **7,** 31–41.

Pêcher, A. (1991). The contact between the higher Himalaya Crystallines and the Tibetan Sedimentary Series: Miocene large-scale dextral shearing. *Tectonics* **10,** 587–598.

Petö, R. (1976). An experimental investigation of melting relations involving muscovite and paragonite in the silica saturated portion of the system $K_2O–Na_2O–SiO_2–H_2O$ to 15 kbar total pressure. *Progress in Experimental Petrology, NERC, London* **3,** 41–52.

Pinet, C. & Jaupart, C. (1987). A thermal model for the distribution in space and time of the Himalayan granites. *Earth and Planetary Science Letters* **84,** 87–99.

Quidelleur, X., Grove, M., Lovera, O. M., Harrison, T. M., Yin, A. & Ryerson, F. J. (1997). The thermal evolution and slip history of the Renbu Zedong thrust, southeastern Tibet. *Journal of Geophysical Research* **102,** 2659–2679.

Rapp, R. P. & Watson, E. B. (1986). Monazite solubility and dissolution kinetics: implications for thorium and light rare earth chemistry of felsic magmas. *Contributions to Mineralogy and Petrology* **94,** 304–316.

Scaillet, B., Pichavant, M. & Roux, J. (1995). Experimental crystallization of leucogranite magmas. *Journal of Petrology* **36,** 663–705.

Schärer, U. (1984). The effect of initial [230]Th disequilibrium on young U–Pb ages: the Makalu case. *Earth and Planetary Science Letters* **67,** 191–204.

Schärer, U. & Allègre, C. J. (1983). The Palung granite (Himalaya); high resolution U–Pb systematics in zircon and monazite. *Earth and Planetary Science Letters* **63,** 423–432.

Schärer, U., Xu, R. H. & Allègre, C. J. (1986). U–(Th)–Pb systematics and ages of Himalayan leucogranites, South Tibet. *Earth and Planetary Science Letters* **77,** 35–48.

Searle, M. P., Parrish, R. R., Hodges, K. V., Hurford, A. J., Ayres, M. W. & Whitehouse, M. J. (1997). Shisha Pangma leucogranite, South Tibetan Himalaya: field relations, geochemistry, age, origin, and emplacement. *Journal of Geology* **105,** 295–317.

Smith, H. A. & Giletti, B. J. (1997). Pb diffusion in monazite. *Geochimica et Cosmochimica Acta* **61,** 1047–1055.

Thompson, A. B. (1982). Dehydration melting of pelitic rocks and the generation of H_2O-undersaturated granitic liquids. *American Journal of Science* **282,** 1567–1595.

Vidal, P. (1978). Rb–Sr systematics in granite from central Nepal (Manaslu): significance of the Oligocene age and high $^{87}Sr/^{86}Sr$ ratio in Himalayan orogeny—Comment. *Geology* **6,** 196.

Vidal, P., Cocherie, A. & Le Fort, P. (1982). Geochemical investigations of the origin of the Manaslu leucogranite (Himalaya, Nepal). *Geochimica et Cosmochimica Acta* **46,** 2279–2292.

Vidal, P., Benard-Griffiths, J., Cocherie, A., Le Fort, P., Peucat, J. J. & Sheppard, S. M. F. (1984). Geochemical comparison between Himalayan leucogranites. *Physics of the Earth and Planetary Interiors* **35,** 179–190.

Villa, I. M. (1996). Age and cooling history of the Manaslu granite: implications for Himalayan tectonics: Comment. *Journal of Volcanology and Geothermal Research* **70,** 255–261.

Watson, E. B. (1996). Dissolution, growth and survival of zircons during crustal fusion: kinetic principles, geologic models and implications for isotopic inheritance. *Transactions of the Royal Society of Edinburgh* **87,** 43–56.

Yin, A. (1993). Mechanics of wedge-shaped blocks I: an elastic solution for compressional wedges. *Journal of Geophysical Research* **98,** 14245–14256.